東南大學圖書館
Southeast University Library

东图学术快报
Academic express of SEU LIB

前沿经典　　学科热点

学术动态　　工具助手

编者按：

2021 年不仅是“十四五”的开局之年，也是两个百年目标交汇与转换之年。为了让我校师生快速了解国内外学术前沿、经典及热点，图书馆学科服务团队特开辟此栏目，利用 WOS/ESI/Incites、Scopus/SciVal 等权威数据库和分析工具筛选研究前沿，或跟踪重要学术网站获取最新学术动态，分专题进行编译报道。我们也面向全校师生征集关注的领域和专题。

本期推荐报道 Nature、Science 期刊上材料科学领域的最新论文。

CONTACT US

联系电话：025-52090336-817

办公地址：李文正图书馆 B401 室

编辑：刘丽娟

审核：陆　美

美国 Science（《科学》）、英国 Nature（《自然》）及美国 Cell（《细胞》）是国际公认的三大享有最高学术声誉的科技期刊，发表在这三大期刊上的论文简称 CNS 论文。本次精选 2021 年 10 月 Science 和 Nature 中的部分物理领域论文，详细情况如下。

物理 10 月 Science 论文

[1] **Direct evidence for Cooper pairing without a spectral gap in a disordered superconductor above Tc**

高于 Tc 的无序超导体中无谱隙库珀对的直接证据

出版信息：SCIENCE 29 Oct 2021，Vol 374, Issue 6567，pp. 608-611

作者：KOEN M. BASTIAANS, DAMIANOS CHATZOPOULOS, JIAN-FENG GE, DOOHEE CHO, WILLEM O. TROMP, JAN M. VAN RUITENBEEK, ET AL.

第一作者单位：Leiden Institute of Physics, Leiden University, 2333 CALeiden, Netherlands.

全文链接：https://www.science.org/doi/10.1126/science.abe3987

Abstract：

The idea that preformed Cooper pairs could exist in a superconductor at temperatures higher than its zero-resistance critical temperature (Tc) has been explored for unconventional, interfacial, and disordered superconductors, but direct experimental evidence is lacking. We used scanning tunneling noise spectroscopy to show that preformed Cooper pairs exist up to temperatures much higher than Tc in the disordered superconductor titanium nitride by observing an enhancement in the shot noise that is equivalent to a change of the effective charge from one to two electron charges. We further show that the spectroscopic gap fills up rather than closes with increasing temperature. Our results demonstrate the existence of a state above Tc that, much like an ordinary metal, has no (pseudo) gap but carries charge through paired electrons.

摘要翻译：

在高于零电阻临界温度（**Tc**）的情况下，超导体中是否存在预先形成的库珀对？人们在非常规超导体、界面超导体和无序超导体中进行了探索，但直接实验证据仍不明确。

通过观察散粒噪声的增强（相当于有效电荷从一个电子电荷变为两个电子电荷），研究组使用扫描隧道噪声谱表明，在无序超导体氮化钛中，温度远高于 **Tc** 时，预先形成的库珀对仍存在。

研究组进一步表明，随着温度升高，光谱间隙会被填满而非闭合。该结果证明存在一种温度高于 **Tc** 的状态，它与普通金属非常相似，没有（赝）能隙，但通过成对电子携带电荷。

文中插图：

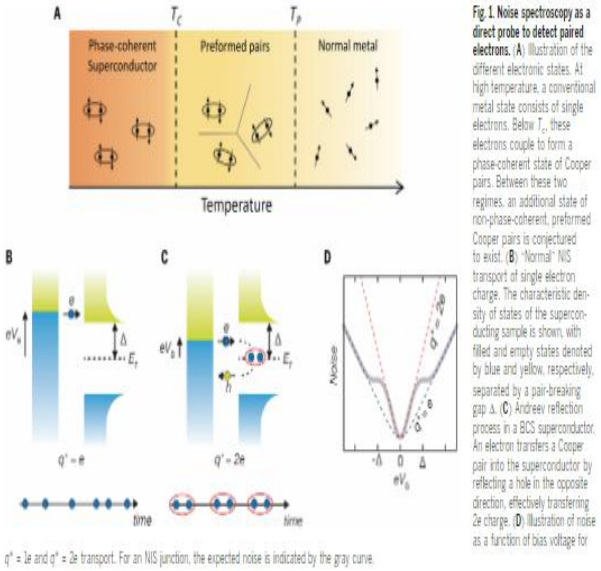

Fig. 1. Noise spectroscopy as a direct probe to detect paired electrons. (**A**) Illustration of the different electronic states. At high temperature, a conventional metal state consists of single electrons. Below T_c, these electrons couple to form a phase-coherent state of Cooper pairs. Between these two regimes, an additional state of non-phase-coherent, preformed Cooper pairs is conjectured to exist. (**B**) "Normal" NIS transport of single electron charge. The characteristic density of states of the superconducting sample is shown, with filled and empty states denoted by blue and yellow, respectively, separated by a pair-breaking gap Δ. (**C**) Andreev reflection process in a BCS superconductor. An electron transfers a Cooper pair into the superconductor by reflecting a hole in the opposite direction, effectively transferring 2e charge. (**D**) Illustration of noise as a function of bias voltage for $q^* = 1e$ and $q^* = 2e$ transport. For an NIS junction, the expected noise is indicated by the gray curve.

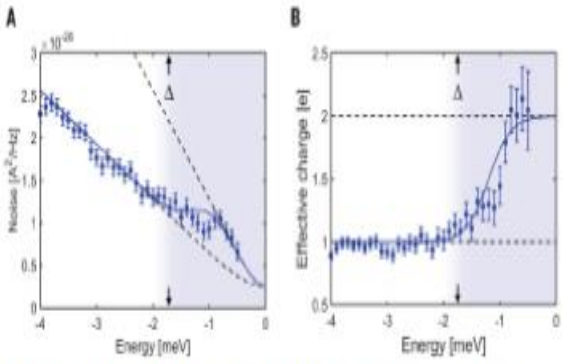

Fig. 2. Evidence for pairing in TiN from scanning noise spectroscopy. (**A**) Noise in the tunneling junction (R_J = 5 MΩ) between the STM tip and TiN sample at 2.3 K, with the thermal amplifier noise subtracted, as function of the bias voltage. (**B**) Spectroscopy of the effective charge $q^*(V)$ at 2.3 K. In both panels, blue points represent experimental data and dashed lines indicate the expected noise for $q^* = 1e$ and $q^* = 2e$. Blue shading indicates the spectral gap observed in the differential conductance (Fig. 4A). The solid blue curves indicate a step from 1e to 2e, broadened by the respective thermal resolution (fig. S8).

[2] **Evolution of water structures in metal-organic frameworks for improved atmospheric water harvesting**

改善大气水收集的金属-有机框架中水结构的演变

出版信息：SCIENCE 22 Oct 2021，Vol 374, Issue 6566，pp. 454-459

作者：NIKITA HANIKEL, XIAOKUN PEI, SAUMIL CHHEDAHAO LYU et al.

第一作者单位：Department of Chemistry and Kavli Energy NanoscienceInstitute, University of California, Berkeley, CA 94720, USA

全文链接：https://www.science.org/doi/10.1126/science.abj0890

Abstract：

Although the positions of water guests in porous crystals can be identified, determination of their filling sequence remains challenging. We deciphered the water-filling mechanism for the state-of-the-art water-harvesting metal-organic framework MOF-303 by performing an extensive series of single-crystal x-ray diffraction measurements and density functional theory calculations. The first water molecules strongly bind to the polar organic linkers; they are followed by additional water molecules forming isolated clusters, then chains of clusters, and finally a water network. This evolution of water structures led us to modify the pores by the multivariate approach, thereby precisely modulating the binding strength of the first water molecules and deliberately shaping the water uptake behavior. This resulted in higher water productivity, as well as tunability of regeneration temperature and enthalpy, without compromising capacity and stability.

摘要翻译：

虽然水在多孔晶体中的位置可以确定，但确定它们的填充顺序仍然具有挑战性。通过进行一系列单晶 x 射线衍射测量和密度泛函理论计算，我们破译了最先进的金属有机框架 MOF-303 的充水机制。

第一个水分子与极性有机连接物紧密结合；接着是额外的水分子形成孤立的簇，然后是簇链，最后形成一个水网络。

这种水结构的进化促使我们通过多元方法改变孔隙，从而精确地调节第一个水分子的结合强度，并调节吸水行为。这导致了更高的水生产率，以及再生温度和焓的可调性，而不影响容量和稳定性。

文中插图：

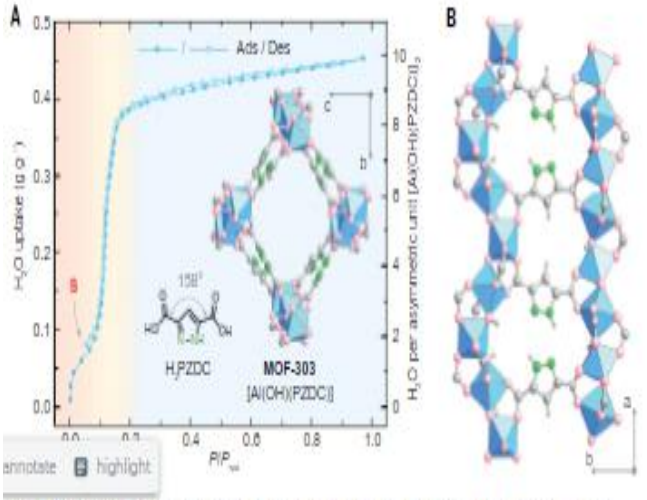

Fig. 1. Water sorption isotherm and crystal structure of MOF-303. (**A**) Water sorption isotherm at 25°C, where *P* is water vapor pressure and P_{sat} is the saturation water vapor pressure. The water uptake is displayed gravimetrically and with respect to the asymmetric unit $[Al(OH)(PZDC)]_2$ of MOF-303. The three segments of the isotherm are highlighted in red, yellow, and blue in the background. The linker 1*H*-3,5-pyrazoledicarboxylic acid (H_2PZDC) and MOF crystal structure are shown in the inset. The initial step is labeled with S. (**B**) Side view visualizing two hydrophilic pockets defined by a pair of pyrazole-based linkers with their nitrogen atoms pointing toward each other and flanked by two aluminum oxide rod-like SBUs. Here and in other figures, coordinate systems are given for guidance. Al, blue polyhedron; O, pink; C and H, gray; N, green.

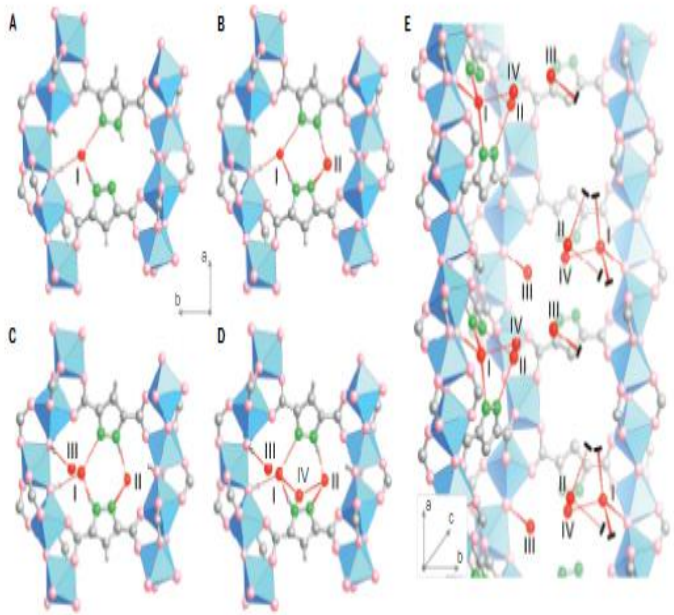

Fig. 2. Crystal structures of the seeding water adsorption sites in MOF-303. (**A** to **D**) Sequential adsorption of the first four water molecules (I to IV) per asymmetric building unit depicted in the hydrophilic pocket, as determined by SCXRD analysis. (**E**) Three-dimensional view of the first four water molecules in the framework pore. Shown crystallographic snapshots were captured at 0.04 g g^{-1} in (A), 0.06 g g^{-1} in (B), 0.11 g g^{-1} in (C), and 0.15 g g^{-1} in (D) and (E). H-bonds are depicted as red dashed lines. Black solid bars at the end of H-bonds in (E) represent binding interactions to the MOF, which is partially omitted for clarity. Al, blue polyhedron; O in the framework structure, pink; O in H_2O, red; C and H, gray; N, green. H atoms in (E) are omitted for clarity.

[3] **A compositional link between rocky exoplanets and their host stars**

系外岩质行星和主恒星之间的组成关联

出版信息：SCIENCE 15 Oct 2021，Vol 374, Issue 6565，pp. 330-332

作者：Vardan Adibekyan, Caroline Dorn, Sérgio G. Sousa, Nuno C. Santos, Bertram Bitsch, Garik Israelian, Christoph Mordasini, etc.

第一作者单位：Instituto de Astrofísica e Ciências do Espaço, Universidadedo Porto, Centro de Astrofísica d a Universidade do Porto,4150-762 Porto, Portugal

全文链接：https://www.science.org/doi/10.1126/science.abg8794

Abstract：

Stars and planets both form by accreting material from a surrounding disk. Because they grow from the same material, theory predicts that there should be a relationship between their compositions. In this study, we search for a compositional link between rocky exoplanets and their host stars. We estimate the iron-mass fraction of rocky exoplanets from their masses and radii and compare it with the compositions of their host stars, which we assume reflect the compositions of the protoplanetary disks. We find a correlation (but not a 1:1 relationship) between these two quantities, with a slope of >4, which we interpret as being attributable to planet formation processes. Super-Earths and super-Mercuries appear to be distinct populations with differing compositions, implying differences in their formation processes.

摘要翻译：

恒星和行星都是通过从周围的圆盘中吸积物质而形成的。因为它们是由相同的物质生长而来，所以理论预测其组成之间应该有一定的关系。作者探寻了系外岩石行星与其主恒星之间的成分联系。

他们从岩石系外行星的质量和半径来估计其铁质量分数，并将其与其主恒星的组成进行比较，假设主恒星反映了原行星盘的组成。他们发现这两个量之间存在相关性（但不是 1:1 的关系），其斜率>4，将其解释为可归因于行星形成过程。

作者表示，“超级地球”和“超级水星”似乎是不同的类型，组成成分不同，这意味着它们的形成过程不同。

文中插图：

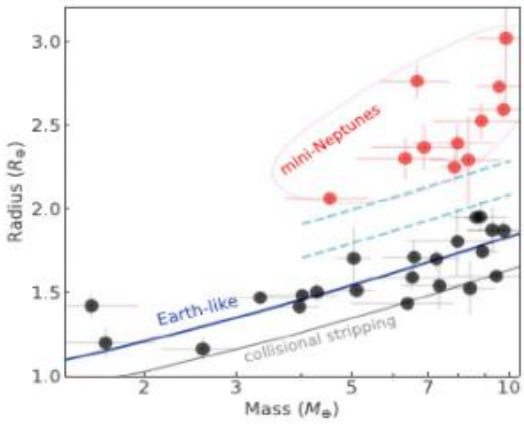

Fig. 1. Mass-radius diagram for the rocky planets in our sample. All planets in our sample have masses below 10 $M_\oplus$ and mass and radius uncertainties of <30%. The radii of the planets are given in Earth radii, $R_\oplus$. The light-blue dashed curves, drawn by eye, indicate the location of the radius gap that separates the mini-Neptunes with gaseous envelopes (red circles) from the planets without gaseous envelopes (black circles). The solid blue curve shows the mass-radius relationship expected for Earth-like composition (32% Fe + 68% $MgSiO_3$) (*18*). The gray solid curve marks the minimum planetary radius predicted by a collisional stripping (giant impact) model (*23*). All error bars show one standard deviation.

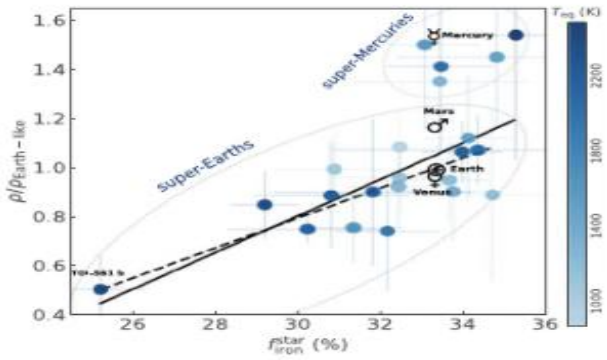

Fig. 2. Densities of rocky planets as a function of iron fraction. The measured density of each planet was normalized by the expected density of an Earth-like composition at that mass (*18*) (Fig. 1). The iron-mass fraction was calculated from the elemental abundances of the host star. The rocky planets in the Solar System are indicated with their respective symbols in black; these all have the same iron fraction because it was derived from the abundances of the Sun, not measured directly from the planets. The black solid and dashed lines show the correlation for the full sample and for the sample after excluding the five potential super-Mercuries, respectively. The Solar System planets are not included in the linear regressions. The exoplanet symbols (blue circles) are color coded by the equilibrium temperature of the planets to search for possible trends. No color gradient is visible. All error bars show one standard deviation.

[4] **Electrically tunable Feshbach resonances in twisted bilayer semiconductors**

双层扭曲半导体中的电可调谐费什巴赫共振

出版信息：SCIENCE 15 Oct 2021，Vol 374, Issue 6565，pp. 336-340

作者：IDO SCHWARTZ, YUYA SHIMAZAKI, CLEMENS KUHLENKAMP, KENJI WATANABE, TAKASHI TANIGUCHI, MARTIN KRONER, AND ATAÇ IMAMOĞLU

第一作者单位：Institute for Quantum Electronics, ETH Zürich, CH-8093Zürich, Switzerland.

全文链接：https://www.science.org/doi/10.1126/science.abj3831

摘要翻译:

过渡金属二卤素双分子层中的莫尔超晶格为研究与光谱学的强相关性提供了一个平台，尽管观察到丰富的 Mott-Wigner 物理源于周期势和库仑相互作用，没有隧道耦合诱导的电子态杂化确保了经典层自由度。

作者研究了 MoSe2 同质层结构，其中层间相干隧穿允许电场控制操纵和基态空穴层赝自旋的测量。作者在激子-空穴散射中观察到一个电可调的二维费什巴赫共振，这使他们能够控制位于不同层中的激子和空穴之间的相互作用强度。

作者表示，该结果可能使具有可调谐相互作用的简并玻色费米混合物的实现成为可能。

Abstract:

Moiré superlattices in transition metal dichalcogenide bilayers provide a platform for exploring strong correlations with optical spectroscopy. Despite the observation of rich Mott-Wigner physics stemming from an interplay between the periodic potential and Coulomb interactions, the absence of tunnel coupling–induced hybridization of electronic states has ensured a classical layer degree of freedom. We investigated a MoSe2 homobilayer structure where interlayer coherent tunneling allows for electric field–controlled manipulation and measurement of the ground-state hole-layer pseudospin. We observed an electrically tunable two-dimensional Feshbach resonance in exciton-hole scattering, which allowed us to control the strength of interactions between excitons and holes located in different layers. Our results may enable the realization of degenerate Bose-Fermi mixtures with tunable interactions.

文中插图：

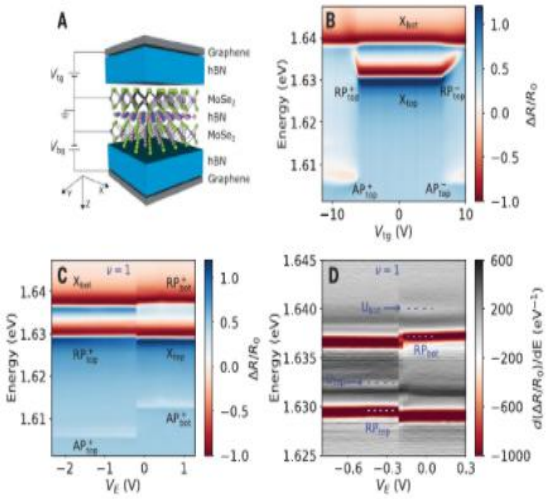

Fig. 1. Device structure and basic characteristics. (**A**) Schematic of the device structure. The applied electric field and the optical axis are along the *z* direction. (**B**) Top gate–dependent differential reflectance spectra at a fixed back-gate voltage V_{bg} = −4 V. X_{top} and X_{bot}, top- and bottom-layer excitons [split as a result of strain (*16*)]; RP^{+}_{top} and RP^{-}_{top}, top-layer positive and negative repulsive polarons; AP^{+}_{top} and AP^{-}_{top}, top-layer positive and negative attractive polarons. (**C**) V_E-dependent differential reflectance spectra at a fixed chemical potential for unity filling of the moiré superlattice ν = 1. RP^{+}_{bot} and AP^{+}_{bot}, bottom-layer positive repulsive and attractive polaron resonances. (**D**) V_E-dependent differential reflectance spectra differentiated with respect to photon energy at a fixed chemical potential for ν = 1. U_{top} and U_{bot}, top- and bottom-layer umklapp resonances. Blue dashed lines mark the energy of the repulsive polarons and the associated umklapp resonances.

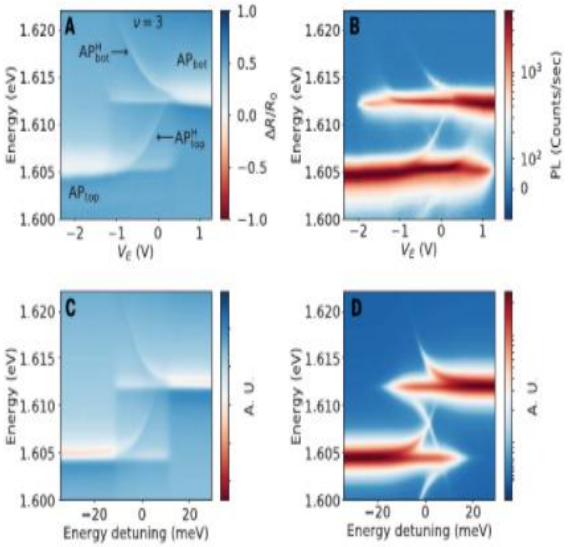

Fig. 2. Coherent hole tunneling at moiré filling factor ν = 3. (**A**) V_E-dependent differential reflectance spectra at a fixed chemical potential for ν = 3, where each lattice site accommodates three holes. AP_{top} and AP_{bot}, top- and bottom-layer attractive polarons; AP^{H}_{top} and AP^{H}_{bot}, top- and bottom-layer attractive polarons originating from the hybridized hole state. (**B**) V_E-dependent PL spectra at a fixed chemical potential for ν = 3. (**C** and **D**) Calculated reflectance spectra (C) and PL (D) at ν = 3 as function of energy detuning between top and bottom layers. A.U., arbitrary units.

[5] **Grain boundary velocity and curvature are not correlated in Ni polycrystals**

镍多晶中晶界速度和曲率不相关

出版信息：SCIENCE 8 Oct 2021，Vol 374, Issue 6564，pp. 189-193

作者：ADITI BHATTACHARYA, YU-FENG SHEN, CHRISTOPHER M. HEFFERAN, SHIU FAI LI, JONATHAN LIND, ROBERT M. SUTER, ET AL.

第一作者单位：Department of Materials Science and Engineering, CarnegieMellon University, Pittsburgh, PA 15213, USA.

全文链接：https://www.science.org/doi/10.1126/science.abj3210

Abstract：

Grain boundary velocity has been believed to be correlated to curvature, and this is an important relationship for modeling how polycrystalline materials coarsen during annealing. We determined the velocities and curvatures of approximately 52,000 grain boundaries in a nickel polycrystal using three-dimensional orientation maps measured by high-energy diffraction microscopy before and after annealing at 800°C. Unexpectedly, the grain boundary velocities and curvatures were uncorrelated. Instead, we found strong correlations between the boundary velocity and the five macroscopic parameters that specify grain boundary crystallography. The sensitivity of the velocity to grain boundary crystallography might be the result of defect-mediated grain boundary migration or the anisotropy of the grain boundary energy. The absence of a correlation between velocity and curvature likely results from the constraints imposed by the grain boundary network and implies the need for a new model for grain boundary migration.

摘要翻译：

晶界速度被认为与曲率有关，这种相关性在模拟多晶材料在退火过程中如何粗化很重要。

研究组使用高能衍射显微镜测量了镍多晶体在 800℃退火前后的三维取向图，并确定了约 52000 个晶界的速度和曲率。

出乎意料的是，晶界速度和曲率并不相关。相反，研究组发现边界速度和五个决定晶界晶体学的宏观参数之间有很强的相关性。

速度对晶界晶体学的敏感性，可能是缺陷介导的晶界迁移或晶界能各向异性的结果。速度和曲率之间缺乏相关性可能是由晶界网络施加的约束造成的，这意味着需要一种新的晶界迁移模型。

文中插图：

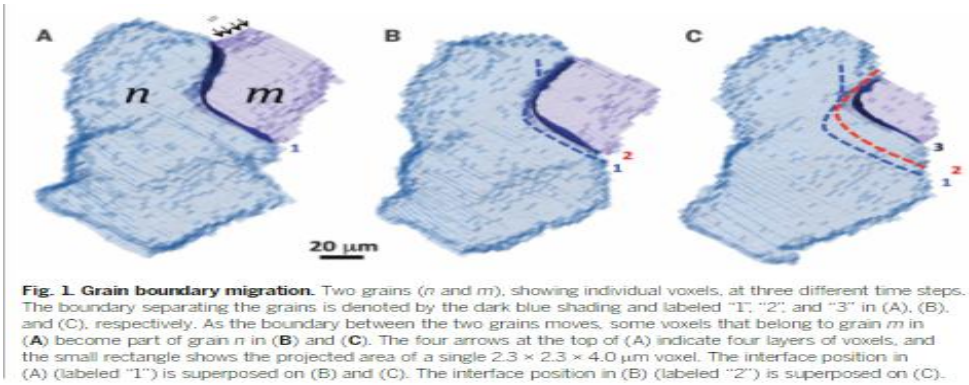

Fig. 1. Grain boundary migration. Two grains (*n* and *m*), showing individual voxels, at three different time steps. The boundary separating the grains is denoted by the dark blue shading and labeled "1", "2", and "3" in (A), (B), and (C), respectively. As the boundary between the two grains moves, some voxels that belong to grain *m* in (**A**) become part of grain *n* in (**B**) and (**C**). The four arrows at the top of (A) indicate four layers of voxels, and the small rectangle shows the projected area of a single 2.3 × 2.3 × 4.0 μm voxel. The interface position in (A) (labeled "1") is superposed on (B) and (C). The interface position in (B) (labeled "2") is superposed on (C).

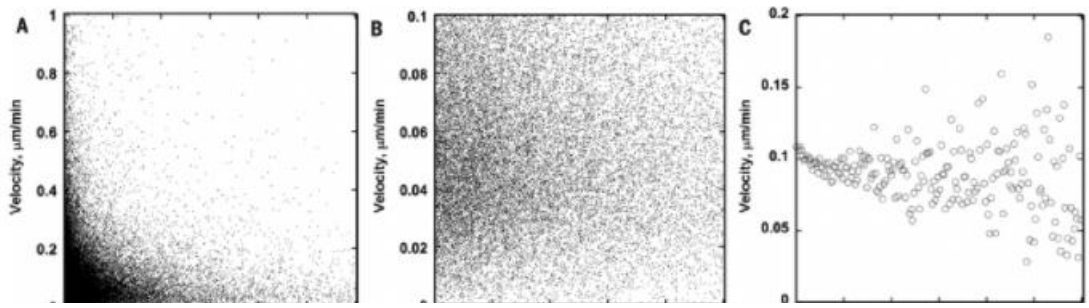

[6] **Levitodynamics: Levitation and control of microscopic objects in vacuum**

悬浮动力学：真空中微观物体的悬浮和控制

出版信息：SCIENCE 8 Oct 2021，Vol 374, Issue 6564

作者：C. GONZALEZ-BALLESTERO, M. ASPELMEYER, L. NOVOTNY, R. QUIDANT, AND O. ROMERO-ISART.

第一作者单位：Institute for Theoretical Physics, University of Innsbruck,A-6020 Innsbruck, Austria.

全文链接：https://www.science.org/doi/10.1126/science.abg3027

Abstract：

The control of levitated nano- and micro-objects in vacuum—which capitalizes on scientific achievements in the fields of atomic physics, control theory, and optomechanics—is of considerable interest. The ability to couple the motion of levitated systems to internal degrees of freedom, as well as to external forces and systems, provides opportunities for science and technology. Attractive research directions, ranging from fundamental quantum physics to commercial sensors, have been unlocked by the many recent experimental achievements, including motional ground-state cooling of an optically levitated nanoparticle. Here we review the status, challenges, and prospects of levitodynamics, the multidisciplinary research area devoted to understanding, controlling, and using levitated nano- and micro-objects in vacuum.

摘要翻译：

利用原子物理、控制理论和光力学领域的科学成果，在真空中控制悬浮的纳米和微观物体是一个相当有趣的课题。

将悬浮系统的运动与内部自由度以及外力和系统相结合的能力为科技提供了机遇。诸多最新实验成果，包括光学悬浮纳米颗粒的运动基态冷却，已解锁了许多吸引人的研究方向，从基础量子物理到商业传感器等。

研究组回顾了悬浮动力学的现状、挑战和前景，这是一个多学科的研究领域，致力于理解、控制和使用真空中悬浮的纳米和微观物体。

文中插图：

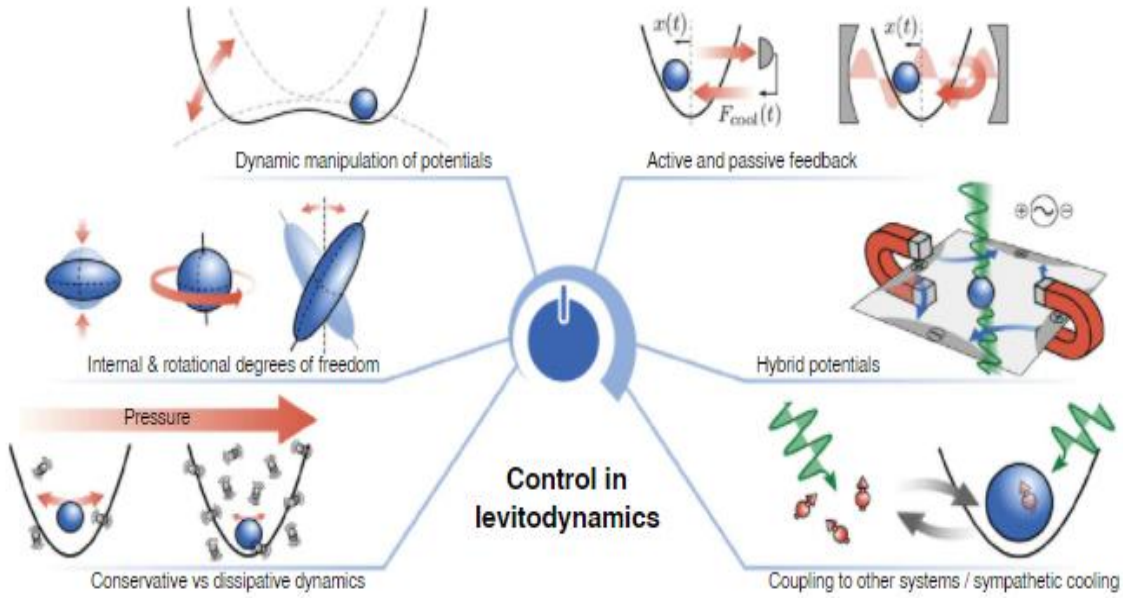

Fig. 1. Control in levitodynamics. The control toolbox of levitodynamics makes it possible to tailor every degree of freedom of a levitated particle in multiple ways. Both the conservative dynamics and the dissipation of motional, rotational, and internal (e.g., acoustic) degrees of freedom can be tailored via dynamic manipulation of potentials and modification of gas pressure, respectively. They can also be cooled and parametrically driven via both active and passive feedback. Additional control can be achieved through hybrid traps and coupling to external systems, which also provide controlled nonlinearity. $F_{cool}(t)$, cooling force.

[1] Fault-tolerant control of an error-corrected qubit

校正量子位的容错控制

出版信息：Nature volume 598, pages281–286 (2021)

作者：Laird Egan, Dripto M. Debroy, Crystal Noel, Andrew Risinger et al.

第一作者单位：Joint Quantum Institute, Center for Quantum Information and Computer Science, University of Maryland, College Park, MD, USA.

全文链接：https://www.nature.com/articles/s41586-021-03928-y

Abstract：

Here we experimentally demonstrate fault-tolerant circuits for the preparation, measurement, rotation and stabilizer measurement of a Bacon–Shor logical qubit using 13 trapped ion qubits. When we compare these fault-tolerant protocols to non-fault-tolerant protocols, we see significant reductions in the error rates of the logical primitives in the presence of noise. The result of fault-tolerant design is an average state preparation and measurement error of 0.6 per cent and a Clifford gate error of 0.3 per cent after offline error correction. In addition, we prepare magic states with fidelities that exceed the distillation threshold, demonstrating all of the key single-qubit ingredients required for universal fault-tolerant control. These results demonstrate that fault-tolerant circuits enable highly accurate logical primitives in current quantum systems. With improved two-qubit gates and the use of intermediate measurements, a stabilized logical qubit can be achieved.

摘要翻译：

在此，我们演示了使用 13 个捕获离子量子位元的 Bacon–Shor 逻辑量子位元的制备、测量、旋转和稳定测量的容错电路。当我们将这些容错协议与非容错协议进行比较时，我们发现在存在噪声的情况下，逻辑原语的错误率显著降低。

容错设计的结果是，离线纠错后，状态准备和测量的平均误差为 0.6%，克利福德门误差为 0.3%。此外，我们演示了通用容错控制所需的所有关键单量子位成分。通过改进的双量子位门和中间测量的使用，可以实现稳定的逻辑量子位。

文中插图：

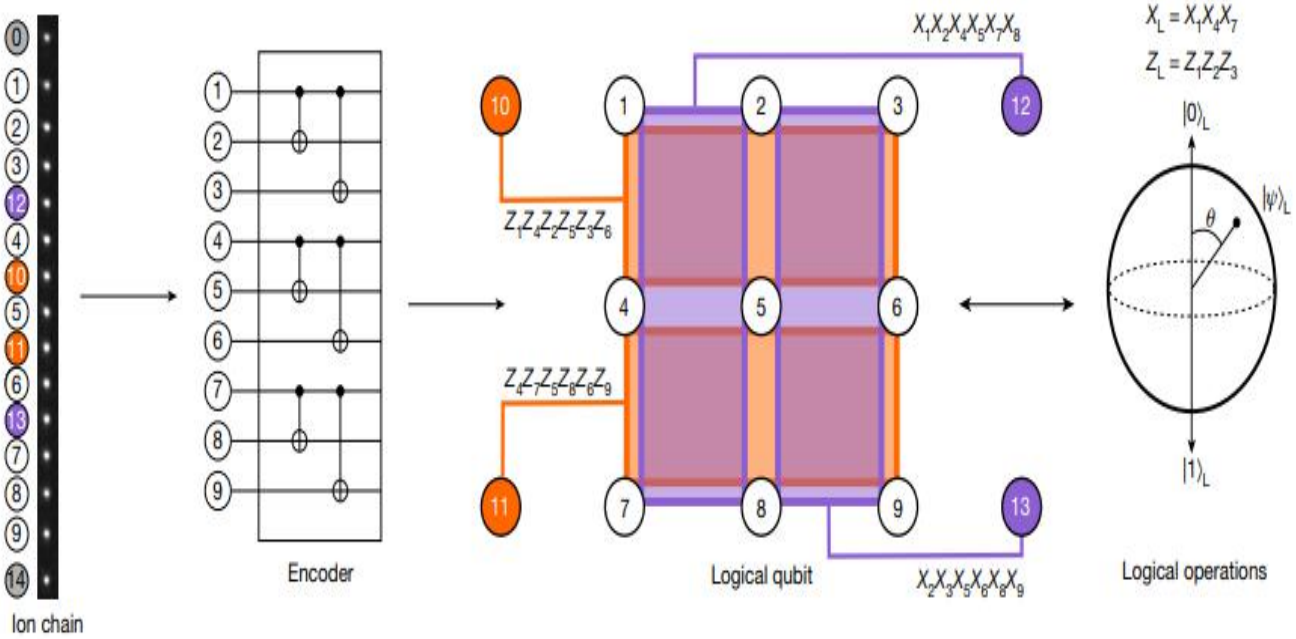

Fig. 1 | The Bacon–Shor subsystem code implemented on a 15-ion chain. Bacon–Shor is a [[9,1,3]] subsystem code that encodes nine data qubits into one logical qubit. Four weight-six stabilizers are mapped to ancillary qubits 10, 11, 12 and 13, for measuring errors in the *X* and *Z* basis. We demonstrate encoding of the logical qubit, with subsequent logical gate operations or error syndrome extraction.

[2] Strongly correlated excitonic insulator in atomic double layers

原子双层中的强相关激子绝缘体

出版信息：Nature volume 598, pages585–589 (2021)

作者：Liguo Ma, Phuong X. Nguyen, Zefang Wang, Yongxin Zeng, Kenji Watanabe, Takashi Taniguchi, Allan H. MacDonald, Kin Fai Mak & Jie Shan

第一作者单位：School of Applied and Engineering Physics, Cornell University, Ithaca, NY, USA

全文链接：https://www.nature.com/articles/s41586-021-03947-9

Abstract：

Excitonic insulators (EIs) arise from the formation of bound electron–hole pairs (excitons) in semiconductors and provide a solid-state platform for quantum many-boson physics. Strong exciton–exciton repulsion is expected to stabilize condensed superfluid and crystalline phases by suppressing both density and phase fluctuations. Although spectroscopic signatures of EIs have been reported, conclusive evidence for strongly correlated EI states has remained elusive. Here we demonstrate a strongly correlated two-dimensional (2D) EI ground state formed in transition metal dichalcogenide (TMD) semiconductor double layers. A quasi-equilibrium spatially indirect exciton fluid is created when the bias voltage applied between the two electrically isolated TMD layers is tuned to a range that populates bound electron–hole pairs, but not free electrons or holes. Capacitance measurements show that the fluid is exciton-compressible but charge-incompressible—direct thermodynamic evidence of the EI. The fluid is also strongly correlated with a dimensionless exciton coupling constant exceeding 10. We construct an exciton phase diagram that reveals both the Mott transition and interaction-stabilized quasi-condensation. Our experiment paves the path for realizing exotic quantum phases of excitons, as well as multi-terminal exciton circuitry for applications.

摘要翻译：

激子绝缘体（EIs）产生于半导体中束缚电子-空穴对（激子）的形成，为量子多玻色子物理提供了一个固态平台。强激子斥力通过抑制密度和相的波动来稳定凝聚的超流体和结晶相。虽然科学家已经报道了 EI 的光谱特征，但强烈相关 EI 状态的确凿证据仍然难以捉摸。

作者演示了过渡金属二卤族（TMD）半导体双层中形成的一个强相关的二维 EI 基态。当施加在两个电隔离 TMD 层之间的偏置电压被调谐到一个范围，该范围会填充束缚电子-空穴对，而不是自由电子或空穴时，就会产生准平衡空间间接激子流体。电容测量表明流体是激可压缩但电荷不可压缩的，这是 EI 的直接热力学证据。

流体也与超过 10 的无因次激子耦合常数密切相关。他们构建了一个激子相图，揭示了莫特跃迁和相互作用稳定的准凝聚。作者表示，该实验为实现奇异的激子量子相位以及多端激子电路的应用铺平了道路。

文中插图:

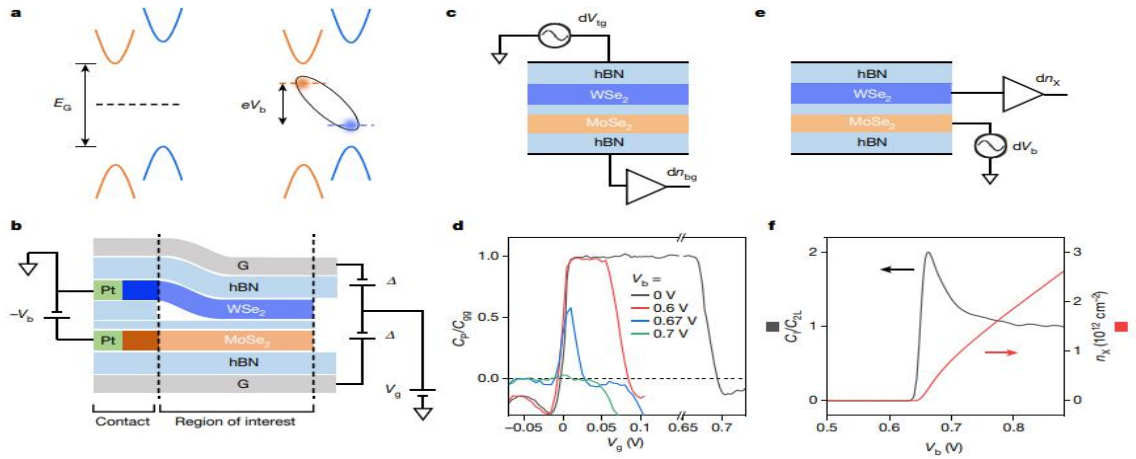

Fig. 1 | Electrical reservoir for interlayer excitons. a, Type II band alignment of $MoSe_2/WSe_2$ double layers with interlayer bandgap E_G (left). A bias voltage V_b across the layers separates the electron and hole chemical potentials (dashed lines) and reduces the charge gap (right). Interlayer excitons are formed spontaneously when the bias voltage, which acts as a chemical potential for excitons, exceeds the exciton energy $E_G - E_B$. **b**, Schematic cross-section of dual-gated double layer devices. The anti-symmetric gating Δ reduces E_G in the region of interest; it closes E_G in the contact region to heavily dope the TMDs. The symmetric gating V_g shifts the electron and hole chemical potentials together and tune their density difference. **c**, **e**, Schematics of the penetration (**c**) and interlayer capacitance (**e**) measurements. The double layer is a.c. grounded in **c**. **d**, Gate dependence of the normalized penetration capacitance at representative bias voltages. The sharp capacitance drops signify electron or hole doping into the double layer. The charge gap is closed for $V_b \approx 0.7$ V. **f**, Bias dependence of the normalized interlayer capacitance (black) and the exciton density (red) at $V_g = 0$. **d** and **f** are measured at 15 K and $\Delta = 4.6$ V.

[3] Observation of fractional edge excitations in nanographene spin chains

纳米石墨烯自旋链中分数阶边激发的观察

出版信息：Nature volume 598, pages287–292 (2021)

作者：Shantanu Mishra, Gonçalo Catarina, Fupeng Wu, Ricardo Ortiz, David Jacob et al.

第一作者单位：Empa—Swiss Federal Laboratories for Materials Science and Technology, Dübendorf, Switzerland.

全文链接：https://www.nature.com/articles/s41586-021-03842-3

Abstract:

Here, we use on-surface synthesis to fabricate one-dimensional spin chains that contain the $S = 1$ polycyclic aromatic hydrocarbon triangulene as the building block. Using scanning tunnelling microscopy and spectroscopy at 4.5 K, we probe length-dependent magnetic excitations at the atomic scale in both open-ended and cyclic spin chains, and directly observe gapped spin excitations and fractional edge states therein. Exact diagonalization calculations provide conclusive evidence that the spin chains are described by the $S = 1$ bilinear-biquadratic Hamiltonian in the Haldane symmetry-protected topological phase. Our results open a bottom-up approach to study strongly correlated phases in purely organic materials, with the potential for the realization of measurement-based quantum computation.

摘要翻译:

在此，我们使用表面合成法合成的一维自旋链，包含 $S = 1$ 多环芳香烃三角烯作为构建块。我们利用扫描隧道显微镜和 4.5 K 下的光谱，在原子尺度上探测了开放自旋链和循环自旋链中长度依赖的磁激发，并直接观察到其中的间隙自旋激发和分数阶边态。

精确的对角化计算提供了决定性的证据，证明自旋链在 Haldane 对称保护拓扑相中是由 $S = 1$ 双线性-双二次哈密顿量描述的。我们的结果开启了一种自下而上的方法来研究纯有机材料中的强相关相，并有可能实现基于测量的量子计算。

文中插图：

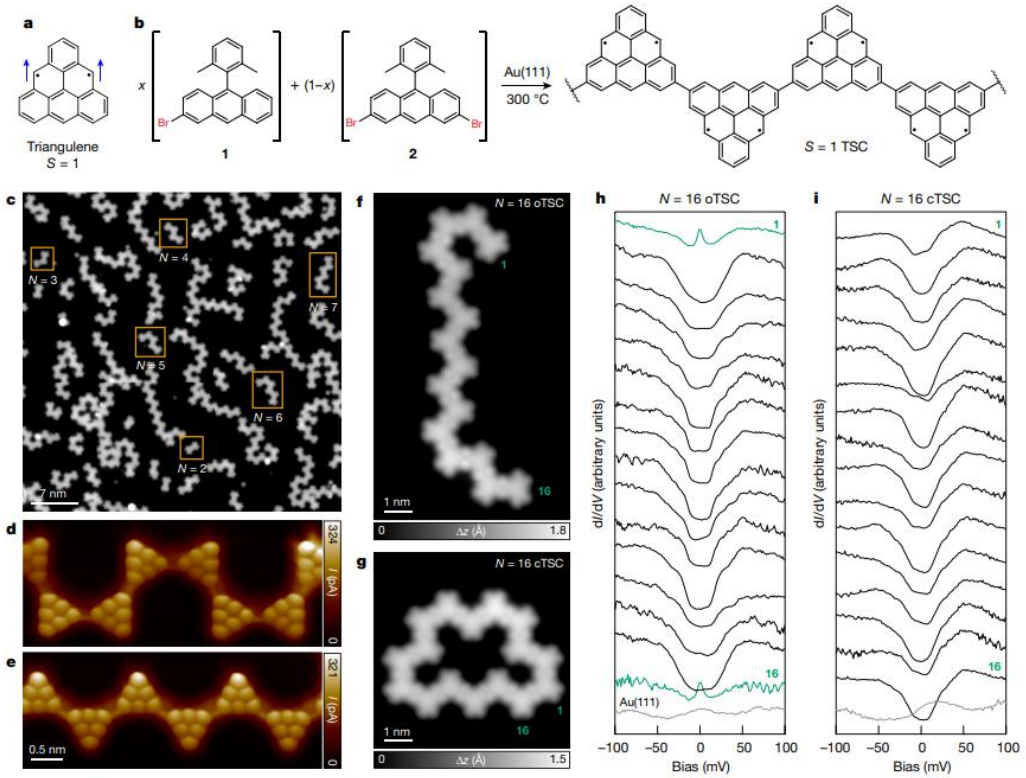

Fig. 1 | On-surface synthesis of triangulene spin chains and observation of zero-energy edge excitations. a, Chemical structure of triangulene. **b**, On-surface synthesis of TSCs using precursor mixture **1** + **2**. **c**, Overview STM image after annealing the precursor mixture ($x = 0.2$) on Au(111) at 300 °C (tunnelling parameters: $V = -0.7$ V, $I = 70$ pA). The image is acquired with a carbon monoxide (CO) functionalized tip. oTSCs with $N = 2$–7 are highlighted. **d**, **e**, Bond-resolved STM images of TSCs with *cis* (**d**) and *trans* (**e**) intertriangulene bonding configurations (open feedback parameters: $V = -5$ mV, $I = 50$ pA; $\Delta h = -0.7$ Å). Δh denotes the offset applied to the tip–sample distance with respect to the STM setpoint above the TSCs. **f**, **g**, High-resolution STM images of $N = 16$ oTSC ($V = -0.6$ V, $I = 200$ pA; **f**) and cTSC ($V = -0.7$ V, $I = 500$ pA; **g**). Δz denotes the apparent height. **h**, **i**, dI/dV spectra acquired on every unit of the $N = 16$ oTSC (**h**) and cTSC (**i**), revealing zero-energy excitations exclusively at the terminal units of the oTSC (green curves). Numerals near the curves indicate the unit number, marked in the high-resolution STM images, on which the corresponding spectrum was acquired. The dI/dV spectra in the panels are offset vertically for visual clarity. Open feedback parameters for the dI/dV spectra: $V = -100$ mV, $I = 1.4$ nA; root mean squared modulation voltage $V_{rms} = 1$ mV.

[4] Fine-regolith production on asteroids controlled by rock porosity

由岩石孔隙度控制的小行星上的细风化层生成

出版信息：Nature volume 598, pages49–52 (2021)

作者：S. Cambioni, M. Delbo, G. Poggiali, C. Avdellidou, A. J. Ryan, J. D. P. Deshapriya, E. Asphaug, R.-L. Ballouz, M. A. Barucci, C. A. Bennett, W. F. Bottke, J. R. Brucato, K. N. Burke, E. Cloutis, D. N. DellaGiustina, J. P. Emery, B. Rozitis, K. J. Walsh & D. S. Lauretta

第一作者单位: Lunar and Planetary Laboratory, University of Arizona, Tucson, AZ, USA.

全文链接：https://www.nature.com/articles/s41586-021-03816-5

Abstract：

Spacecraft missions have observed regolith blankets of unconsolidated subcentimetre particles on stony asteroids. Telescopic data have suggested the presence of regolith blankets also on carbonaceous asteroids, including (101955) Bennu and (162173) Ryugu. However, despite observations of processes that are capable of comminuting boulders into unconsolidated materials, such as meteoroid bombardment and thermal cracking, Bennu and Ryugu lack extensive areas covered in subcentimetre particles. Here we report an inverse correlation between the local abundance of subcentimetre particles and the porosity of rocks on Bennu. We interpret this finding to mean that accumulation of unconsolidated subcentimetre particles is frustrated where the rocks are highly porous, which appears to be most of the surface. The highly porous rocks are compressed rather than fragmented by meteoroid impacts, consistent with laboratory experiments, and thermal cracking proceeds more slowly than in denser rocks. We infer that regolith blankets are uncommon on carbonaceous asteroids, which are the most numerous type of asteroid. By contrast, these terrains should be common on stony asteroids, which have less porous rocks and are the second-most populous group by composition. The higher porosity of carbonaceous asteroid materials may have aided in their compaction and cementation to form breccias, which dominate the carbonaceous chondrite meteorites.

摘要翻译：

宇宙飞船已经在多岩石的小行星上观测到由松散的亚厘米粒子组成的风化层。望远镜数据表明，碳质小行星上也存在风化层，包括（101955）本努小行星和（162173）龙宫小行星。

然而，尽管观测到一些过程，如流星体轰击和热裂能够将巨石粉碎成松散的物质，但本努和龙宫缺乏覆盖着亚厘米以下颗粒的广阔区域。

作者报告了亚厘米颗粒的局部丰度与本努岩石孔隙度之间的反相关关系。他们把这一发现解释为，在岩石多孔性很强的地方，松散的亚厘米级颗粒的积聚受到阻碍。高孔隙度的岩石在流星体的撞击下被压缩而不是破碎，这与实验室的实验结果一致。热裂比密度较大的岩石进行得慢。

作者推断，风化层在碳质小行星上并不常见，而碳质小行星是数量最多的小行星类型。相比之下，这些地形在多石的小行星上应该很常见，因为这些小行星的岩石孔隙较少，按组成来看是第二多的小行星。碳质小行星物质较高的孔隙度可能有助于其压实和胶结形成角砾岩，这些角砾岩以碳质球粒陨石为主。

文中插图：

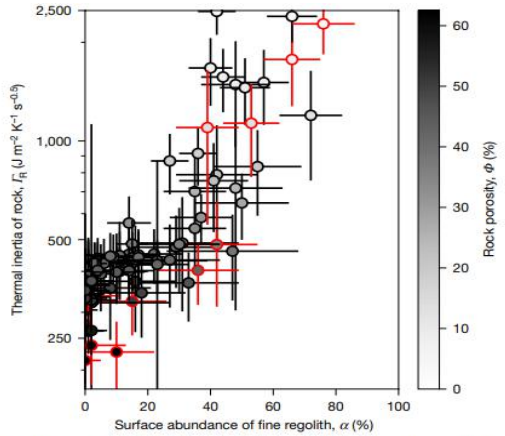

Fig. 1 | The thermal inertia of Bennu's rocks is positively correlated with the local surface abundance of fine regolith. The grey shading of the data corresponds to the porosity Φ estimated from Γ_R (Methods). The red points correspond to 13 areas where α could be overestimated because of the presence[10] of boulders for which Γ_R could be lower than the threshold value between fine regolith and rocks (Methods). The plotted data have a goodness of fit of $\chi^2_r < 3$ (Methods), which is satisfactory for these types of observation. The error bars correspond to one standard deviation (Supplementary Table 1, Methods), computed from about 670 samples on average.

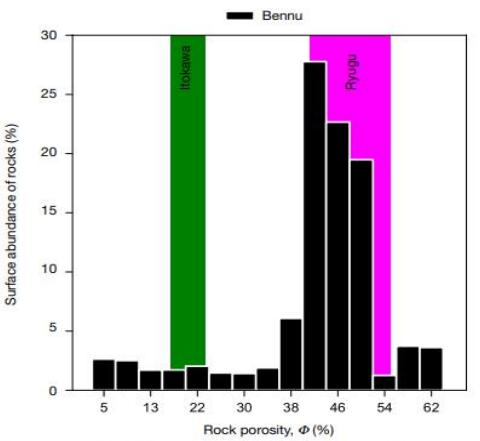

Fig. 2 | The porosities of most of Bennu's and Ryugu's rocks are much higher than that of Itokawa's rocks. The porosities of Bennu's rocks are weighted according to rock abundance ($1-\alpha$) and binned using the Freedman–Diaconis rule. The magenta and green shaded areas indicate the estimated surface-averaged ranges of rock porosity on Ryugu[18,19] and Itokawa[17], respectively. About 70% of the rocks on Bennu are as porous as those on Ryugu, whereas only about 5% of Bennu's rocks have porosity similar to that of Itokawa's rocks.

[5] Quantum anomalous Hall octet driven by orbital magnetism in bilayer graphene

双层石墨烯的轨道磁性驱动的量子反常霍尔八隅体

出版信息：Nature volume 598, pages53–58 (2021)

作者：Fabian R. Geisenhof, Felix Winterer, Anna M. Seiler, Jakob Lenz, Tianyi Xu, Fan Zhang & R. Thomas Weitz

第一作者单位：Physics of Nanosystems, Department of Physics, Ludwig-Maximilians-Universität München, Munich, Germany.

全文链接：https://www.nature.com/articles/s41586-021-03849-w

Abstract：

The quantum anomalous Hall (QAH) effect—a macroscopic manifestation of chiral band topology at zero magnetic field—has been experimentally realized only by the magnetic doping of topological insulators and the delicate design of moiré heterostructures. However, the seemingly simple bilayer graphene without magnetic doping or moiré engineering has long been predicted to host competing ordered states with QAH effects. Here we explore states in bilayer graphene with a conductance of 2 e2h−1 (where e is the electronic charge and h is Planck's constant) that not only survive down to anomalously small magnetic fields and up to temperatures of five kelvin but also exhibit magnetic hysteresis. Together, the experimental signatures provide compelling evidence for orbital-magnetism-driven QAH behaviour that is tunable via electric and magnetic fields as well as carrier sign.

摘要翻译：

量子反常霍尔（QAH）效应是零磁场下手性能带拓扑结构的宏观表现，仅通过拓扑绝缘体 s 的磁掺杂和 moiré异质结构的精细设计，就可以实验实现。然而，没有磁性掺杂或 moiré工程的看似简单的双层石墨烯长期以来被预测具有 QAH 效应的竞争性有序态。

作者探索了电导为 2 e2h−1（其中 e 为电荷，h 为普朗克常数）的双层石墨烯的状态，这种状态不仅能在异常小的磁场和 5 开氏温度下存活，而且还表现出磁滞现象。作者表示，这些实验特征为轨道磁驱动的 QAH 行为提供了令人信服的证据，这种行为可以通过电场、磁场以及载波特征来调节。

文中插图：

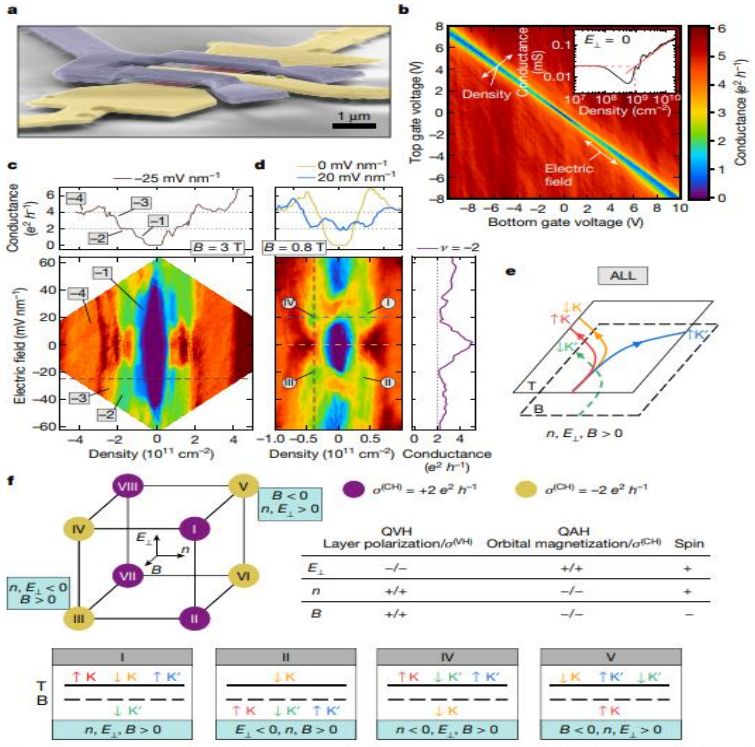

Fig. 1 | Exchange-interaction-driven quantum Hall states in dually gated, freestanding bilayer graphene. a, False-colour scanning electron microscope image of a suspended bilayer graphene device. Contacts, top gate and bilayer graphene are shown in yellow, blue and red, respectively. **b**, Conductance map as a function of top gate voltage and bottom gate voltage at $B = 0$ and $T < 10$ mK. Inset: conductance as a function of charge carrier density at $E_\perp = 0$. The red lines are linear fits and the dashed red lines are guides to the eye, indicating the residual charge carrier inhomogeneity in the device. **c**, **d**, Maps of the conductance as a function of $E_\perp$ and n at $B = 3$ T (**c**) and $B = 0.8$ T (**d**). The roman numerals in **d** label the 'ALL' phases labelled by the same numerals in **f**. **e**, Schematic representation of one 'ALL' QAH phase showing the classical counterpart of its corresponding spontaneous quantum Hall effect for $n, E_\perp, B > 0$. T and B refer to the top and bottom graphene layers, respectively. **f**, Top: schematic of the eight different 'ALL' phases and their corresponding Hall conductance $\sigma^{(CH)}$ and how they can be accessed by tuning n, $E_\perp$ and/or B. The table shows the properties of the QVH and QAH species of the 'ALL' octet: the layer polarization and orbital magnetization as well as the valley and charge Hall conductivities, $\sigma^{(VH)}$ and $\sigma^{(CH)}$. +/− indicates whether the observables are even/odd under flipping n, $E_\perp$ or B. Bottom: schematics of the layer polarizations of the four spin–valley species for four exemplary 'ALL' phases.

[6] Topological complex-energy braiding of non-Hermitian bands

非厄米带的拓扑复能编织

出版信息：Nature volume 598, pages59–64 (2021)

作者：Kai Wang, Avik Dutt, Charles C. Wojcik & Shanhui Fan

第一作者单位：Ginzton Laboratory and Department of Electrical Engineering, Stanford University, Stanford, CA, USA.

全文链接：https://www.nature.com/articles/s41586-021-03848-x

Abstract：

Effects connected with the mathematical theory of knots emerge in many areas of science, from physics to biology. Recent theoretical work discovered that the braid group characterizes the topology of non-Hermitian periodic systems, where the complex band energies can braid in momentum space. However, such braids of complex-energy bands have not been realized or controlled experimentally. Here, we introduce a tight-binding lattice model that can achieve arbitrary elements in the braid group of two strands. We experimentally demonstrate such topological complex-energy braiding of non-Hermitian bands in a synthetic dimension6,7. Our experiments utilize frequency modes in two coupled ring resonators, one of which undergoes simultaneous phase and amplitude modulation. We observe a wide variety of two-band braiding structures that constitute representative instances of links and knots, including the unlink, the unknot, the Hopf link and the trefoil. We also show that the handedness of braids can be changed. Our results provide a direct demonstration of the braid-group characterization of non-Hermitian topology and open a pathway for designing and realizing topologically robust phases in open classical and quantum systems.

摘要翻译：

与“结”的数学理论有关的效应出现在科学的许多领域，从物理学到生物学。最近的理论工作发现，结群表征了非厄米周期系统的拓扑结构，其中复杂能带能量可以在动量空间中编织。

然而，这种复杂能带的编织还没有在实验中实现或控制。作者引入了一个紧绑定晶格模型，它可以实现两股编织群中的任意元素。他们用实验证明了这种拓扑复能编织的非厄米带的合成维数为。

作者表示，该实验利用两个耦合环谐振器中的频率模式，其中一个环谐振器同时进行相位和幅度调制。结果观察到各种各样的双带编织结构，它们构成了链接和结的典型实例。

研究还表明，结的手性是可以改变的。作者表示，该结果直接证明了非厄米拓扑的编织群表征，并为设计和实现开放经典和量子系统的拓扑稳健相开辟了一条途径。

文中插图：

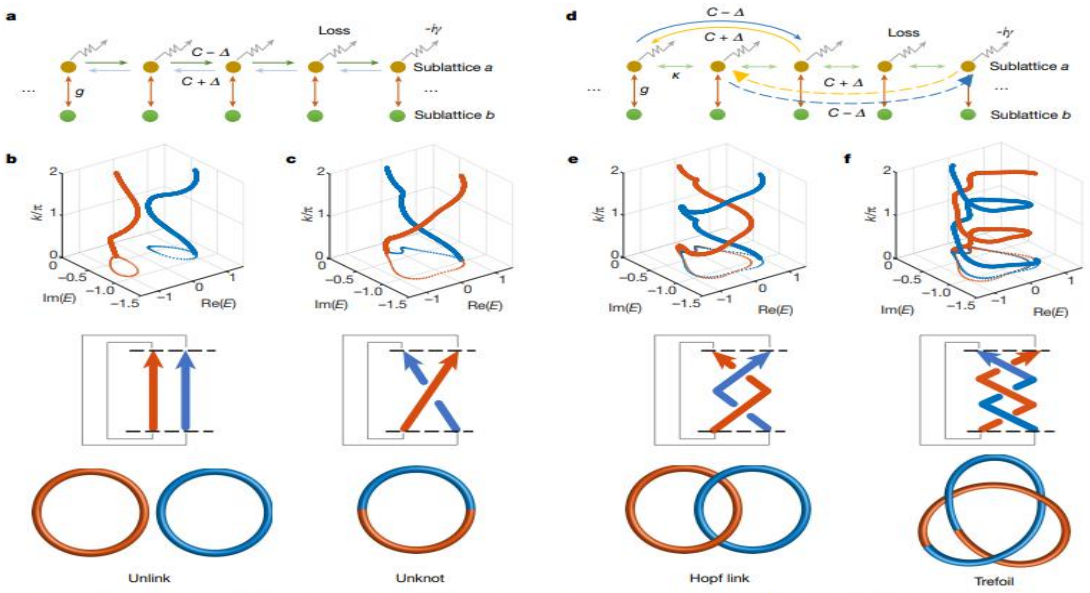

Fig. 1 | Braiding of two non-Hermitian bands. a, Sketch of two-band lattice model with $m = 1$. **b**,**c**, Top, two examples of complex band-energy braiding in the (Re(E), Im(E), k)-space for the lattice model in **a** with a specific choice of parameters, and the dotted curves are projections of the bands in the $k = 0$ plane. Middle, corresponding braid diagrams with braid closures by the grey lines. Bottom, corresponding knot diagrams. **d**, Sketch of two-band lattice model with $m = 2$ (curved solid arrows show second-order coupling) and $m = 3$ (curved dashed arrows show third-order coupling). **e**,**f**, Same as **b**,**c**, but for the model sketched in **d** in the cases of $m = 2$ (**e**) and $m = 3$ (**f**) for specific choices of parameters.